frontiers | Frontiers in Energy Research

TYPE Original Research
PUBLISHED 10 August 2023
DOI 10.3389/fenrg.2023.1244699

OPEN ACCESS

EDITED BY
T. Maiyalagan,
SRM Institute of Science and Technology, India

REVIEWED BY
Fulai Zhao,
Tianjin University, China
Mike Tebyetekerwa,
The University of Queensland, Australia

*CORRESPONDENCE
Youssef Bakkour,
ybakkour@kku.edu.sa
Abdelghani Benyoucef,
a.benyoucel@univ-mascara.dz

RECEIVED 27 June 2023
ACCEPTED 01 August 2023
PUBLISHED 10 August 2023

CITATION
Zenasni M, Belhadj H, Kiari M, Alelyani M, Alhailiy AB, Benyoucef A and Bakkour Y (2023), Synthesis, characterization, and enhanced electrochemical behavior of polypyrrole doped ZrO_2–ZnO electrode materials for supercapacitor applications. *Front. Energy Res.* 11:1244699. doi: 10.3389/fenrg.2023.1244699

Synthesis, characterization, and enhanced electrochemical behavior of polypyrrole doped ZrO_2–ZnO electrode materials for supercapacitor applications

Mounya Zenasni[1], Hafida Belhadj[2], Mohamed Kiari[3], Magbool Alelyani[4], Ali B. Alhailiy[5], Abdelghani Benyoucef[6]* and Youssef Bakkour[4]*

[1]Department of Electrical Engineering, University Djillali Liabès of Sidi Bel Abbès, Sidi Bel Abbès, Algeria, [2]Faculty of Sciences and Technology, University of Mustapha Stambouli, Mascara, Algeria, [3]Department of Chemical and Physical Sciences, Materials Institute, University of Alicante (UA), Alicante, Spain, [4]Department of Radiological Sciences, College of Applied Medical Science, King Khalid University, Abha, Saudi Arabia, [5]Department of Radiology and Medical Imaging, College of Applied Medical Sciences, Prince Sattam Bin Abdulaziz University, Al Kharj, Saudi Arabia, [6]LSTE Laboratory, University of Mustapha Stambouli, Mascara, Algeria

The polypyrrole@ZrO_2–ZnO (PPy@ZrO_2–ZnO) electrodes were synthesized using an *in situ* chemical oxidative method. The samples were characterized by XRD, FTIR, XPS, UV-vis, TGA, and BET. In addition, the electrochemical characteristics of the electrodes are tested by cyclic voltammetry (CV), galvanostatic charge and discharge (G.C.D.), and electrochemical impedance spectroscopy (E.I.S.). The values of the specific capacitances and the energy densities of PPy@ZrO_2–ZnO (1.0) and PPy@ZrO_2–ZnO (0.5) at a current density of 0.5 A g^{-1} are recorded as (395.3 F g^{-1} and 508.5 Wh·kg^{-1}) and (195.3 F g^{-1} and 351.5 Wh·kg^{-1}), respectively. Furthermore, the electrode stability for the formed samples was also determined, which exhibited specific capacitance retention at 90.2% for PPy@ZrO_2–ZnO (1.0) and 82.4% for PPy@ZrO_2–ZnO (0.5) after cycling up to 4,000 cycles. This work provides an efficient approach to the potential of the synthesized samples for application as electrodes in a supercapacitor.

KEYWORDS

polypyrrole, zirconium dioxide, zinc oxide, electrochemical, supercapacitors

1 Introduction

There is a growing need to develop energy storage devices to keep pace with the exponential increase in manufacturing and use of different electronic devices (Augustyn et al., 2014; Mahato et al., 2022). Recent technologies and innovations present better and upgraded versions of these devices and appliances, which likewise request the upgradation of effectiveness of the energy stockpiling materials. Supercapacitors (SCs) are divided into pseudocapacitors (PCs), electric double-layer capacitors, and hybrid supercapacitors (Xiangyu You et al., 2018; Kyunghwa Kim et al., 2019; Liang et al., 2022; Nolly et al., 2022). The PCs have drawn in scientists as of late because of their high power density, energy density, and important cycle life (Bhattarai et al., 2022; Gautam et al., 2022). PCs can be used to store energy faradaically by conducting polymers or inorganic materials applied as

electrodes (Belhadj et al., 2022; Boutaleb et al., 2022; Okhay and Tkach, 2022). These fast surface oxidation/reduction reactions occur through the charging/discharging performance, which usually results in high charge stocked in PCs compared to electric double-layer capacitors in cost of low electronic conductivity (Okhay and Tkach, 2022). Thus, it is necessary to develop novel methods to enhance the electrochemical performance of electrodes. An efficient method is the creation of accessible pores and active sites in the hybrid material's structure. A well-balanced porous structure between microporosity and mesoporosity is generally obtained by the decoration of metal oxide particles with a conducting polymer matrix.

Generally, the most suitable type of electrode materials for PCs are i) carbon-based materials, ii) metal oxides, and iii) conducting polymers (Rehman et al., 2021; Bettucci et al., 2022; Li et al., 2023). However, carbon-based electrode materials have a low energy density, which limits the energy storage mechanism (Bettucci et al., 2022). In this regard, conducting polymer-based transition metal oxides/rare earth oxides, nanocomposites can enhance specific capacitance and consequently improve the energy density (Rehman et al., 2021; Bettucci et al., 2022). Furthermore, conductive polymers, especially polyaniline (PAni), polypyrrole (PPy), and polythiophene (PTh), have wide applications in electronics (Mantione et al., 2017; Zheng et al., 2019), chemical sensors (Azharudeen et al., 2020; Benchikh et al., 2022), antistatic coatings (Dubey et al., 2022), water purifier (Bryan et al., 2016), and energy storage devices (Rehman et al., 2021; Li et al., 2023) in the future. Among these polymers, PPy have attracted much attention because of their scientific interest and technology because it offers advantages like redox property, high conductivity, higher environment stability, and easy preparation (Yamani et al., 2019; Rehman et al., 2021).

Zirconia (ZrO_2) has exceptional electronic characteristics, thanks to its low band gap and the presence of oxygen-containing functional groups. In addition, due to its high hydrophilicity and thermal stability, ZrO_2 significantly enhances the electrochemical performance of the electrode and electrode wettability. Moreover, ZrO_2 nanoparticles are effective among metal oxides into sandwiching with organic matrices, creating extreme technological pertinence, enhanced strength, toughness modification, excellent resisting capability of chemicals and microbes, and corrosion. ZrO_2 is a p-type semiconductor with a large band gap and manifests plentiful oxygen vacancies. It is a good catalyst, owing to enhanced redox activity and strengthened ion exchange proportions (Selvi et al., 2015; Hoseong Han et al., 2019). The ZrO_2 insulating asset and its extensive thermostable behavior have applications in nanoelectronic devices, fuel cells, and gas sensing of oxygen and nitrogen oxide (Adam et al., 2018; Hoseong Han et al., 2019; Sirajul et al., 2021). An excellent optical and electrical domain of zirconia nanoparticles is highly attentive in the broad range of applications corresponding to electro-optic, dielectric, and piezoelectric devices. Furthermore, zinc oxide (ZnO), as one of the more attractive structural and multifunctional products, is widely investigated in electronic devices due to its good electrical conductivity and optoelectronic properties. In addition, ZnO has high electron mobility and powerful mechanical support as a result of its perfect chemical and thermal stabilities (Handayani et al., 2022; Huriya et al., 2023); it is a transition metal oxide with good electrochemical activity and high specific energy density for supercapacitor applications (Huriya et al., 2023). In addition, ZnO and ZrO_2 materials have been co-prepared to render hybrid composites suitable for different applications. For example, Sirajul et al. (2021) successfully prepared a multifunctional ZnO–ZrO_2 heterojunction using the extract of rubber leaves as reducing and capping agents. Shokufeh et al. (2021) synthesized ZnO/ZrO_2/MMT nanocomposites and investigated their performance toward the degradation of Congo red. Jijie et al. (2017) reported a ZnO–ZrO_2 catalyst, which can attain methanol selectivity with CO_2 single-pass. Ayodeji and Simón (2019) created the ZrO_2–ZnO nanoparticles using a sol–gel method, and their antibacterial activity was evaluated. Likewise, in order to gain advanced supercapacitors' performances, the concept of the three-component or ternary system by combining these three components has been proposed. Palsaniya et al. (2021) synthesized PANI-RGO-ZnO ternary nanocomposites by *in situ* polymerization, yielding specific energy and specific power of ~5.61 Wh·kg^{-1} and ~403 W kg^{-1}, respectively. Chee et al. (2015) synthesized ternary polypyrrole/graphene oxide/zinc oxide supercapacitor electrodes and measured their gravimetric capacitance in the two-electrode system to be 94.6 F g^{-1} at 1 A g^{-1}. Ishaq et al. (2019) prepared an rGO/$MnFe_2O_4$/Ppy composite, which demonstrated the gravimetric capacitance and areal capacitance of 232 F g^{-1} and 395 mF cm^{-2}, respectively. Lim et al. (2014) reported a ternary polypyrrole/graphene/nano manganese oxide composite; the gravimetric capacitance of the synthesized composite was 320.6 F g^{-1} at 1 mV s^{-1}. These studies clearly indicate that the design of multi-component composite electrodes for supercapacitors is a beneficial and promising approach that is able to significantly improve the performance of supercapacitors.

In the present study, a composite of ZrO_2 and ZnO, to take advantage of both, for superior electrochemical properties, is prepared using the *in situ* polymerization synthesis method of the PPy matrix. Analytical methods such as Fourier-transform infrared spectroscopy (FTIR), X-ray photoelectron spectroscopy (XPS), X-ray diffraction (XRD), thermal gravimetric analysis (TGA), UV-Visible spectra (UV-Vis), and Brunauer–Emmett–Teller (BET) were used to analyze the synthesized materials. Moreover, the electroactivity of electrodes has been studied by cyclic voltammetry (CV). The electrode developed in this work could be a most promising alternative to repeated storage of electrical energy.

2 Materials and methods

2.1 Materials

The reagents, zinc sulfate heptahydrate ($ZnSO_4$•$5H_2O$), zirconium oxide (ZrO_2), ammoniumpersulfate (APS), pyrrole (Py), poly(vinylidene fluoride) (PVDF; (CH_2CF_2)n) ammonia solution (NH_4OH), N-methyl-2-pyrrolidone (NMP; C_5H_9NO), and hydrochloric acid (HCl) were purchased from Aldrich Chemical Co., Spain, and were utilized as received without any further purifications. Sodium hydroxide (NaOH) and ethanol (C_2H_5OH) were obtained from Merck (Italy). Deionized (DI) water was used to prepare all the solutions.

2.2 Experimental procedure

2.2.1 Synthesis of the ZrO_2–ZnO binary composite

The ZrO_2–ZnO composite was prepared, as reported by Arote et al. (2019). At first, 0.2 g of ZrO_2 was dispersed in 25 mL of the aqueous solution of $ZnSO_4$ and stirred continuously for about 1 h, followed by further addition of 0.25 M NaOH dropwise into the solution in order to adjust their pH in solution to 10. The reactions were carried out in an ultrasonic bath at 55°C. Finally, the resulting ZrO_2–ZnO composite was washed three times with C_2H_5OH by centrifugation in order to remove the impurities, followed by vacuum drying at 400°C for 2 h.

2.2.2 Synthesis of the PPy@ZrO_2-ZnO ternary composite

PPy@ZrO_2–ZnO was prepared by *in situ* chemical oxidation of the Py monomer in the existence of ZrO_2–ZnO using APS as an oxidant in an acidic medium. A typical manufacturing process for PPy@ZrO_2–ZnO is as follows: 1.0 g Py was added to dispersion of 50 mL of 1 M HCl with 5 and 10 wt% incorporation of ZrO_2–ZnO [wt% of the organic–inorganic hybrid, as reported by Rawal et al. (2016)] under ultrasonic action to decrease the aggregation of ZrO_2–ZnO. After 30 min, 3.4 g APS (dissolved in 50 mL of 1 M HCl) was injected into the aforementioned solution with continuous stirring. The resultant mixture was reacted at room temperature for 24 h. The product was filtered and washed with HCl and DW for removing all unreacted particles. The sample was dried in vacuum at 60°C for 24 h (Yamani et al., 2019; Rehman et al., 2021; Belhadj et al., 2022; Handayani et al., 2022).

2.3 Characterization methods

The prepared samples were analyzed using various characterization equipment. The X-ray diffractometer (Bruker CCDApex diffractometer; United States) was used to analyze the crystallite size and geometry of the materials. The surface compositions were tested by X-ray photoelectron spectroscopy (XPS) analyses (ThermoScientific, Kyoto, Japan), using a monochromatic 150-W Al X-ray source. FTIR (Bruker Instruments, Karlsruhe, Germany) was probed to analyze the functional groups in the range of 500–4,000 cm^{-1}. The samples were checked by UV-vis spectroscopy (Hitachi-U3000 spectrophotometer, Japan). Using BET, the surface area, pore size, and volumes were estimated (Quantachrome Instruments version 5.21). The materials were subjected to thermogravimetric analysis using a HitachiSTA7200 instrument under a nitrogen atmosphere.

Electrical conductivity measurements were carried out using LucasLab equipment with four probes in-line. The pellets of 13 mm of diameter were prepared under a pressure of 10Tn cm^{-2}.

2.4 Electrochemical measurements

Cyclic voltammograms (CVs) and the impedance test were determined through the three-electrode system using an eDAQ Potentiostat coupled to an EG&GParc Model175 wave generator. Here, measurements were conducted in HCl (1 M) with a reversible hydrogen electrode (RHE) and platinum foil as the reference electrode and counter electrode, respectively.

3 Results and discussion

3.1 Structural study

XRD was utilized for the estimation of the crystallite size and the nature of the samples. The XRD spectra of PPy, ZrO_2, ZrO_2–ZnO, and PPy@ZrO_2–ZnO (0.5) with (0.5 g) and (1.0 g) composition are presented in Figure 1A. The intense peaks of ZrO_2 exhibit the crystalline nature, whereas the broad hump in the case of PPy shows the amorphous nature. There is a shift occurring upon the addition of ZnO to ZrO_2, indicating that new angle peaks of strain were observed in the ZrO_2–ZnO sample. Moreover, after preparation of ZrO_2–ZnO on the PPy matrix, the diffractograms indicated peaks, suggesting that PPy was the phase found and that the ZrO_2–ZnO crystalline phase was also present. The peaks at angle two theta of PPy are 23.28°, and the corresponding (hkl) values are (100) (Arote et al., 2019; Benchikh et al., 2022) and the peaks at angles 24.01°, 24.39°, 28.13°, 31.42°, 34.12°, 36.07°, 40.69°, 44.82°, 47.38°, 26.84°, 63.11°, and 78.44° with corresponding (hkl) values (011), (110), (−111), (111), (002), (101), (−211), (112), (102), (110), (103), and (112) (Ayodeji and Simón, 2019; Yamani et al., 2019), respectively, indicate the crystalline nature of ZrO_2–ZnO material (Ayodeji and Simón, 2019; Palsaniya et al., 2021). The crystallite sizes of the samples were calculated by Sherrer's formula given as follows (Handayani et al., 2022):

$$D = \frac{0.9\lambda}{\beta \cos \theta},$$

where the average crystallite size is denoted by D, the wavelength of X-ray is represented by λ, full width at half maxima is denoted by β, and Bragg's angle is represented by θ for the diffraction peaks in 2θ starting from 0.9° to 70°. The estimated crystallite sizes of PPy, ZnO_2, ZnO_2–ZnO, and PPy@ZnO_2–ZnO with (0.5 g) and (1.0 g) were found to be 35.7, 29.8, 31.2, 65.5, and 68.4 nm, respectively.

FTIR spectra of PPy, ZnO_2, ZnO_2–ZnO, and PPy@ZnO_2–ZnO are presented in Figure 1B. The spectrum of PPy clearly exhibits the absorption peaks at 1,602 and 1,556 cm^{-1} are attributed to stretch modes of C=C and the Py ring (Umer et al., 2020; Hammadi et al., 2021). The specific peak at 1,405 cm^{-1} is ascribed to be the C–N group (Hammadi et al., 2021). Furthermore, the band at 1,026 cm^{-1} of S=O is assigned to the APS oxidant (Umer et al., 2020). These results confirm that the synthesized polymer was coherent with previous investigations. Moreover, the peaks that appeared in the region 511–744 cm^{-1} are attributed to the Zr–O and Zn–O–Zr vibrational modes (Li et al., 2016), which shows the formation of ZrO_2–ZnO.

The survey XPS spectra of samples provide further wealthy information about the surface elements and chemical status, and Table 1 summarizes the suggested assignments for the found signals of all samples synthesized. Figure 2 shows the change of elements during the synthesis process; the C and N elements' peak represents the PPy matrix; and the O, Zr, and Zn elements' peak represents ZrO_2–ZnO The abovementioned typical peaks appeared in PPy

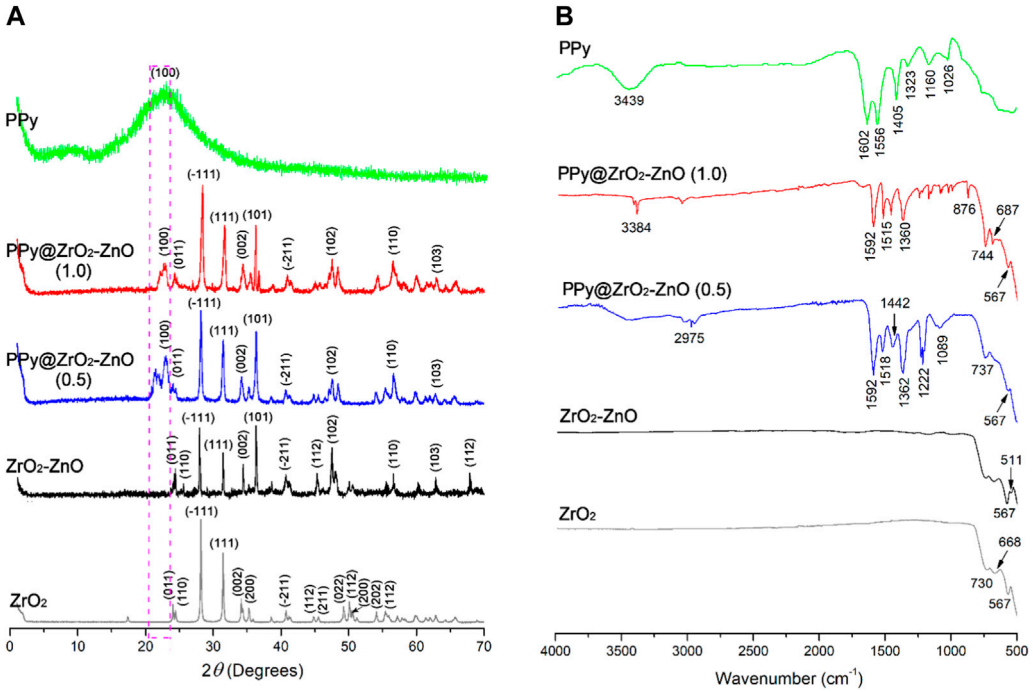

FIGURE 1
(A) XRD patterns and **(B)** FTIR analysis of samples.

TABLE 1 Summary of the XPS binding energy values (eVs) obtained for samples synthesized.

Material	Binding energy (eV)								
	C1s			N1s			O1s		
PPy@ZrO_2–ZnO (0.5)	284.57	286.72	288.29	398.02	399.54	401.11	530.82	532.50	533.49
PPy@ZrO_2–ZnO (1.0)	284.50	286.70	288.30	—	399.60	401.27	530.75	532.17	533.37
PPy	284.66	286.81	288.73	397.95	499.39	401.05	—	—	—
Assignments	C–C C=C	=C–N^+	C=N	=N–	–NH–	–N^+– =N^+–	ZrO_2–ZnO	Zr–OH	O_2
	C–H		–C=N^+		–NC–			Zn–OH	H_2O

@ZrO_2–ZnO (0.5 and 1.0) materials, which indicated that polymers were deposited on the surface of ZrO_2–ZnO, and PPy@ZrO_2–ZnO composites were successfully formed. Furthermore, Figures 3A, B show the N1s narrow scan XPS spectrum of PPy@ZrO_2–ZnO (0.5), and the N1s could be fitted into three peaks of 398.02, 399.54, and 401.11 eV, corresponding to =N–, –NH–, and –NH^+ bonds, respectively. In Figure 3B, the first peak related to PPy@ZrO_2–ZnO (0.5) has disappeared, indicating that a greater ratio of metal ions existed in the PPy@ZrO_2–ZnO (1.0) material. In addition, Table 2 shows the elemental components of the samples found from the survey scan, and the doping report determined the ratio of the oxidized to the neutral N atoms defined through curves fitting of the N1s spectra. Moreover, the high-energy resolution spectra of the C1s peak for PPy@ZrO_2–ZnO (0.5 and 1.0) were individually displayed in Figures 3C, D, respectively. Clearly, from Figure 3A, the spectra of PPy@ZrO_2–ZnO (0.5) were composed of three component peaks at 284.57 (C–C and C–H), 286.72 (=C–N^+), and 288.29 eV (–C=N^+). For PPy@ZrO_2–ZnO (1.0), the binding energy of (=C–N^+ and –C=N^+) did not shift visibly, but the relative intensity decreased moderately compared to the spectra of PPy@ZrO_2–ZnO (0.5); this relates to increasing interactions between the polymer and the amount of ZrO_2–ZnO added. Furthermore, the doping level (DL) was measured from the area ratios of high binding energy bands to the global band area and the defect densities from the area ratios of the low binding energies band to the global band areas. The DL of PPy@ZrO_2–ZnO (0.5) is 0.82, and the FD is only 0.11; while the DL and FD of PPy@ZrO_2–ZnO (1.0) were 0.23 and 0.79, respectively. Thus, the electrode (0.5) has an adequate DL and weak FD that probably offers in its fast charge/discharge ratios and great capacitance. Likewise, the corresponding XPS spectrum of O1s is shown in Figures 3E, F. The most intense band at 530.82 eV corresponds to lattice oxygen in ZrO_2–ZnO (Wang et al., 2012; Obaidullah et al., 2018). The second peak centered at 532.5 eV is

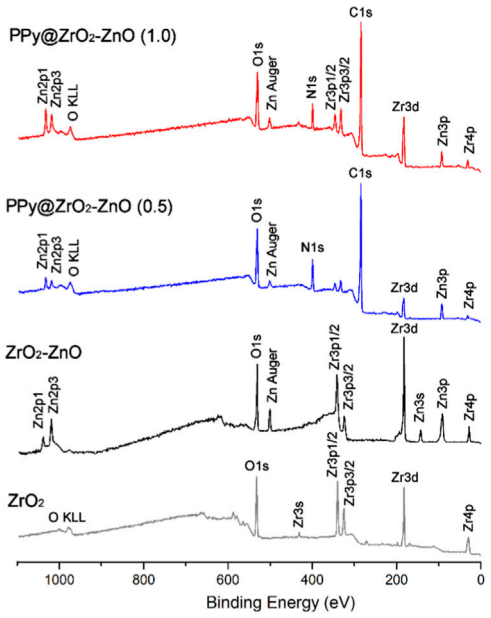

FIGURE 2
Survey XPS spectra of samples.

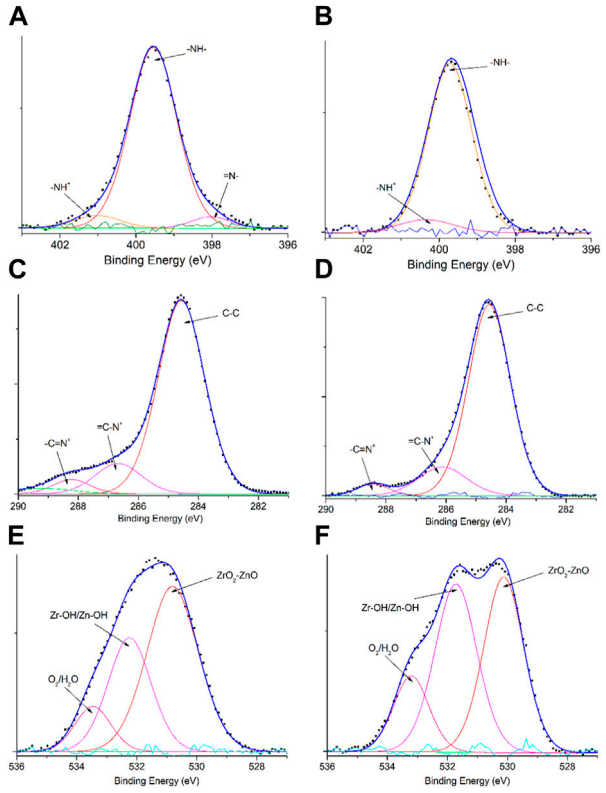

FIGURE 3
XPS spectral signals: **(A)** N1s of PPy@ZrO_2–ZnO (0.5); **(B)** N1s of PPy@ZrO_2–ZnO (1.0); **(C)** C1s of PPy@ZrO_2–ZnO (0.5); **(D)** C1s of PPy@ZrO_2–ZnO (1.0); **(E)** O1s of PPy@ZrO_2–ZnO (0.5); and **(F)** O1s of PPy@ZrO_2–ZnO (1.0).

assigned to hydroxyl groups (Zr–OH/Zn–OH). Some authors have indeed reported the formation of a $Zn(OH)_2$ passive layer in ZnO NPs in contact with air (Filho et al., 1994). Finally, the peak at 533.49 eV is usually attributed to chemisorbed oxygen and water on the surface of the ZrO_2–ZnO composite. It can be seen that the intensity of the Zr–OH/Zn–OH band is higher in the material with PPy@ZrO_2–ZnO (1.0). We speculate that this peak is principally connected to the ZrO_2–ZnO amount added in an excessive amount.

The BET method was used to determine the specific surface areas and pore volumes of samples using the nitrogen adsorption–desorption isotherm, as shown in Figure 4. The surface area and pore radius values of ZrO_2–ZnO are 93.82 $m^2\,g^{-1}$ and 25.73 nm, respectively, and their values in the case of PPy@ZrO_2–ZnO (1.0) are 78.35 $m^2\,g^{-1}$ and 18.76 nm, respectively. Moreover, the results showed that the specific surface area of PPy@ZrO_2–ZnO (0.5) was 71.92 $m^2\,g^{-1}$ with the pore volume around 16.43 nm. The higher surface area of PPy@ZrO_2–ZnO (0.5 and 1.0), as compared to pure PPy (36.21 $m^2\,g^{-1}$ and 13.91 nm), is due to the doping of ZrO_2–ZnO to the polymer surface (Quintana et al., 2017).

Figure 5A shows the absorbance spectra of PPy and PPy@ZrO_2–ZnO (0.5 and 1.0) samples. The peaks at 307, 311, and 312 nm can be associated with the π-conjugated structure of pyrrole rings, and the peaks at 546, 602, and 611 nm can be ascribed to the polypyrrole's chain related to π–π^* transition. As the amount of the ZrO_2–ZnO composite increased, the π–π^* transition red shifted with the reduction in the spectra of materials. This reduction can be associated with the interaction and aggregation of ZrO_2–ZnO within the polymer matrix (Parveen et al., 2016).

The optical bandgap energy for materials was measured by Tauc's relationship between the absorbance coefficient (a) and bandgap (E_g), as shown as follows:

$$(ah\nu)^n = B\left(h\nu - E_g\right),$$

where a, $h\nu$, and E_g denote the absorption coefficient, energy of the photon, and the bandgap energy, respectively. The plot of $(ah\nu)^2$ *vs.* E_g is shown in Figure 5B to determine the band gap energy of samples. The tangent line drawn to the x-axis indicates the bandgap energies of the materials. The estimated bandgap energies for PPy, PPy@ZrO_2–ZnO (0.5), and PPy@ZrO_2–ZnO (1.0) were found to be 2.99, 3.09 and 3.16 eV, respectively. This red shift in energy bandgap may be due to distortion of defects produced in the polymer chain (Ching et al., 2015).

Thermal analyses of samples have been performed to check the stability under a nitrogen atmosphere by using TGA in temperatures in the range from 25°C to 900°C, as shown in Figure 6. Weight loss analysis of the prepared samples was observed in three regions. The first step is up to 170°C having a mass loss of 14.26%, 16.01%, and 3.32% for PPy, PPy@ZrO_2–ZnO (0.5), and PPy@ZrO_2–ZnO (1.0), respectively; which is due to the evaporation of the physical H_2O adsorbed on the surface of the materials (Arote et al., 2019; Yamani et al., 2019; Benchikh et al., 2022). The following steps' region is between 250°C and 510°C having a mass loss of 45.62% for PPy, 22.32% for PPy@ZrO_2–ZnO (0.5), and 15.51% for PPy@ZrO_2–ZnO (1.0) due to the removal of lattice water (Arote et al., 2019; Yamani et al., 2019; Boutaleb et al., 2022). The third region is between 630°C and 900°C due to gradual decomposition of materials. Moreover, the

TABLE 2 Surface elemental composition (%) and the doping ratio of the materials measured with XPS.

Material	C	N	O	Zr	Zn	Loss on ignition	N^+/N	Conductivity ($S.cm^{-1}$)
PPy@ZrO_2–ZnO (0.5)	47.1	13.3	25.3	3.7	2.8	7.8	0.31	1.97
PPy@ZrO_2–ZnO (1.0)	42.8	11.6	31.3	4.9	3.6	5.8	0.82	3.14
PPy	67.2	21.9	4.7	—	—	6.2	0.22	0.87

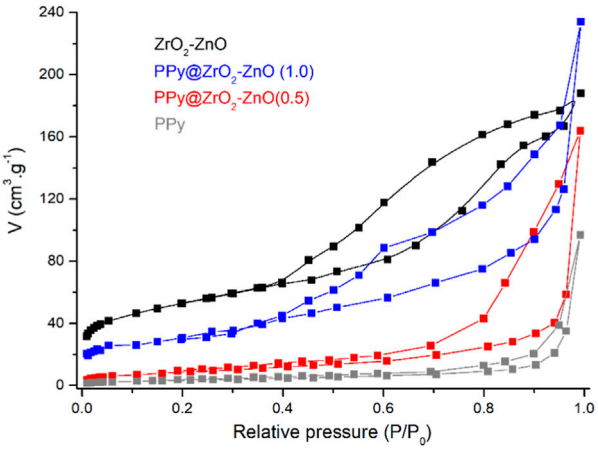

FIGURE 4
BET surface area of materials.

ZrO_2–ZnO composite is the most stable over the entire range of temperatures; however, PPy is the least stable. Upon the addition of ZrO_2–ZnO to the polymer matrix, the stability of PPy@ZrO_2–ZnO (0.5 and 1.0) has been improved.

3.2 Conductivity study

The electrical conductivity was calculated with four probes, and the conductivity values of samples were determined between 0.87 and 3.14 S cm^{-1}. Furthermore, the conductivity of materials increased as the amount of the ZrO_2–ZnO composite to the PPy matrix, as shown in Table 2. Therefore, the higher content of ZrO_2–ZnO increases the conductivity of PPy@ZrO_2–ZnO. The higher conductivity diminishes in response to the separation between the cathodic and the anodic peaks.

3.3 Electrochemical experiments

3.3.1 Cyclic voltammetry study of modified electrodes

Electrochemical properties are a departure point for testing a total approach to interrogating electrolytes for electrochemical storage devices and their related applications, such as sensors in electric vehicles, rechargeable batteries, super capacitors, and smart electronic technology devices. The current study's electrochemical analysis included impedance, dielectric, amperometry, and voltammetry measurements.

The electrochemical tests of electrodes were carried out in HCl (1 M). The dispersion solutions of the different materials were deposited on the electrode surface, and the solvent NMP was evaporated with an infrared lamp. The modified electrode is used as a working electrode. The platinum wire is used as a counter electrode. All potentials were determined against a RHE immersed in the working solution as the reference electrode.

These electrodes were also analyzed by CVs to examine the application of these materials as electrodes in 1 M HCl between −0.1 and 1.0 V at a scan rate of 50 mV s^{-1}. Figure 7 shows the CVs of the modified electrodes. The voltammetric behavior of PPy displayed one redox pair of quasi-reversible at 490 mV is less intense and 410 mV occurs from PPy being oxidized from its neutral state PPy^0 (from the emeraldine state) to PPy^+ (from the pernigraniline state) and on reduction from PPy^+ to PPy^0. Furthermore, the CV plot for PPy@ZrO_2–ZnO (1.0) exhibits a nearly ideal rectangular shape with a large area representing better capacitive property compared to the shape of other electrodes. Moreover, the CV plot for PPy@ZrO_2–ZnO (1.0) exhibits a nearly ideal rectangular shape with a large area representing better capacitive property compared to the shape of the PPy electrode. Moreover, the potential window for PPy@ZrO_2–ZnO (1.0) displayed a symmetric shape, and in addition, the current density presents a growing trend. The high surface area, porosity, and ZrO_2–ZnO composite acting as channels may be the cause for capacitance improvement in the PPy@ZrO_2–ZnO (1.0) electrode. The ions from HCl could insert/desert into/from ZrO_2–ZnO acting as channels between the PPy matrix to store or release energy. Such a way of permeation of these ions into the polymer backbone results in great loading of these ions in the small pores. This strong confinement would furnish a deformed solvated ionic shell that conducts a perfect interaction between the entire PPy chain, which acts as electrodes and the trapped charged ions of the electrolyte, leading to a rise in the values of the supercapacitances (Anastassakis et al., 1990; Raveesha et al., 2019). Importantly, it can be said that the capacitance of PPy@ZrO_2–ZnO (1.0) in the HCl electrolyte generally arises from the creation of an electrical double layer. It formed from the reversible adsorption/desorption of the ions occurring inside the spacers of the ZrO_2–ZnO composite and PPy matrix. The porous ZrO_2–ZnO composite in the ternary composite affords excellent energy storage capacity by holding the polymer backbone collapsing and aggregating. In addition, the conducting ZrO_2–ZnO permits the electrons' transport and easy ion diffusion into the PPy matrix (Raveesha et al., 2019). Conversely, the CV response was less electroactive for the ZrO_2–ZnO composite than that for PPy@ZrO_2–ZnO (0.5 and 1.0) due to the absence of the PPy matrix. For the ZnO-based electrode, the CV response decreased dramatically in comparison to that of all other samples.

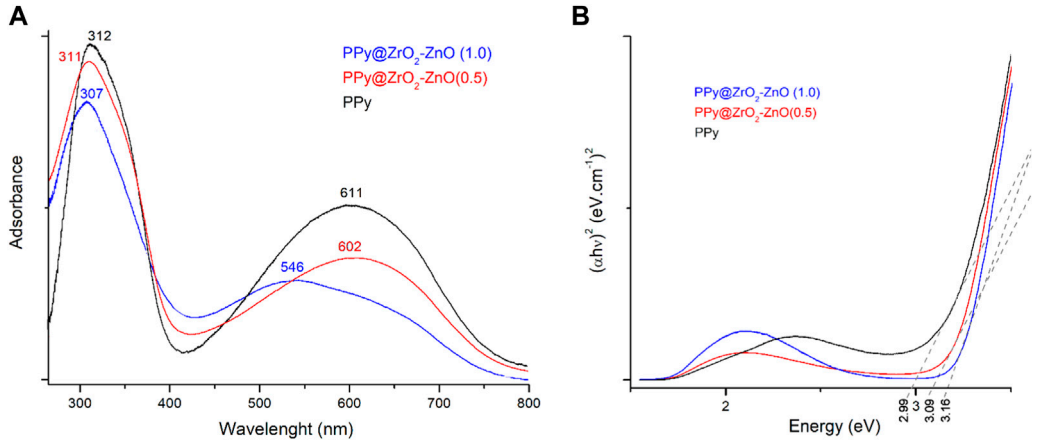

FIGURE 5
(A) UV-vis spectroscopy absorption spectra and **(B)** Tauc plots of materials.

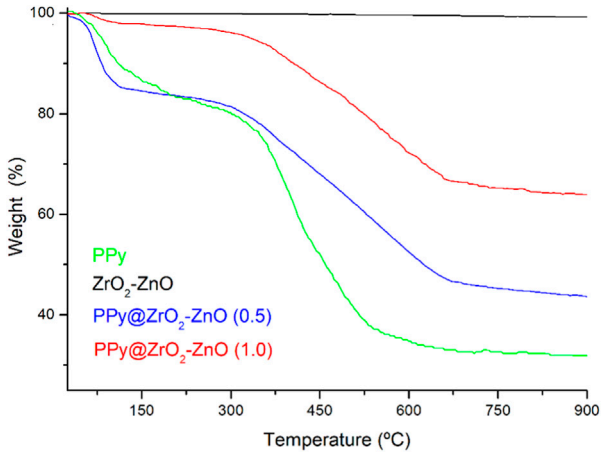

FIGURE 6
TGA curves of materials.

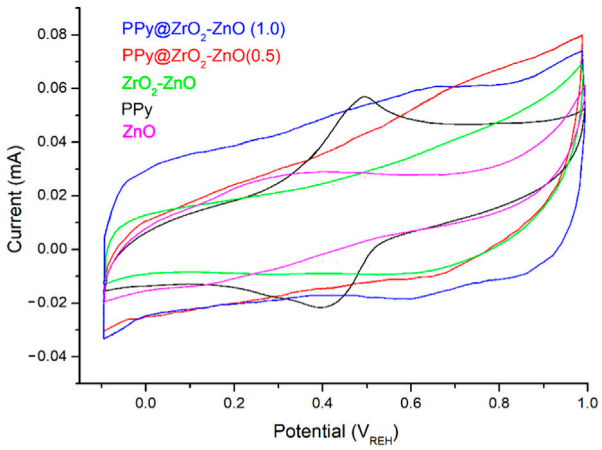

FIGURE 7
Cyclic voltammetry (CV) curves of materials dropped on a glassy carbon electrode in the HCl solution (1 M) at a scan rate 50 mV s^{-1}.

3.3.2 Electrochemical performances

CV testing of the electrodes was carried out in 1 M HCl at scan rates from 5 to 50 mV s^{-1} (Figure 8). The electrodes displayed rectangular CV curves, indicating good capacitive behaviors and fast response times for the PPy@ZrO_2–ZnO (0.5 and 1.0) samples. Since the charge current is related to the scan rates, the current augmented with scan in every CV curve (Ullah et al., 2021). The PPy@ZrO_2–ZnO (1.0) electrode exhibits a greater CV area than those of PPy@ZrO_2–ZnO (0.5), as shown in Figure 8A. As the ZrO_2–ZnO composite size rises, the interconnectivity between the polymer matrix and ZrO_2–ZnO is enhanced (Ullah et al., 2021). Thus, the material with an augmentation ZrO_2–ZnO molecular weight permitted greater current flow in the electrodes. Furthermore, the porous morphology of PPy@ZrO_2–ZnO (1.0) may give a wider surface area for interacting with ions in the electrodes, as demonstrated in Figure 8B.

To further comprehend the impact of ZrO_2–ZnO on the capacitive performances of the PPy@ZrO_2–ZnO supercapacitor, GCD testing of the electrodes was carried out by 4,000 charge–discharge cycles at different current densities of 0.5, 1.0, 1.5, and 2.0 A g^{-1} for a voltage range between −0.1 and 1.0 V. For the GCD graphs, the charge–discharge graphs were symmetric, and such symmetrical shapes of the charge–discharge graphs are indicative of the stabilized currents (Hoseong Han et al., 2019; Ullah et al., 2021). Compared to PPy@ZrO_2–ZnO (0.5), PPy@ZrO_2–ZnO (1.0) displayed longer discharge times for all current values (Figure 9). This suggests that PPy@ZrO_2–ZnO (1.0), which has a greater particle size, presents better electrical characteristics and elevated charge storage properties relative to PPy@ZrO_2–ZnO (0.5) (Han and Cho, 2018; Hoseong Han et al., 2019). According to the formula of Butler–Volmer, the side reactions augment with current densities. Due to the increase in secondary reactions at higher current densities, the discharge time of the electrodes reduced with the growing current density (Cho et al., 2015). Particularly, the electrodes of PPy@ZrO_2–ZnO

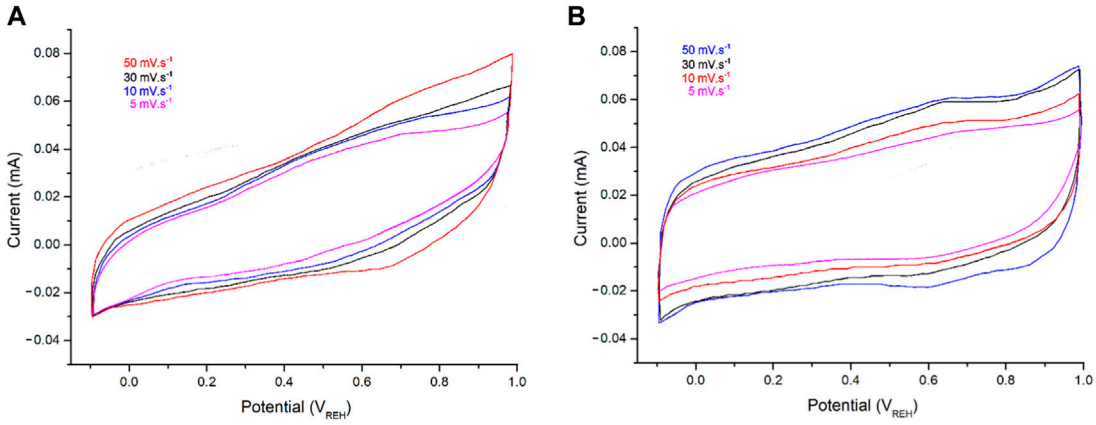

FIGURE 8
Cyclic voltammetry (CV) curves: **(A)** PPy@ZrO_2–ZnO (0.5) and **(B)** PPy@ZrO_2–ZnO (1.0) in HCl solution (1 M) at different scan rates.

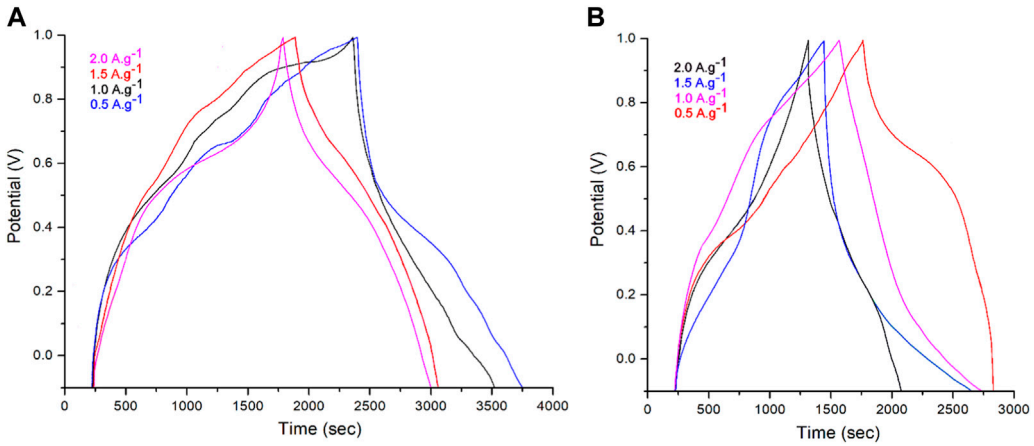

FIGURE 9
(A) Galvanostatic charge/discharge (GCD) curves of the PPy@ZrO_2–ZnO (1.0) electrode; **(B)** GCD curves of the PPy@ZrO_2–ZnO (0.5) electrode at current densities.

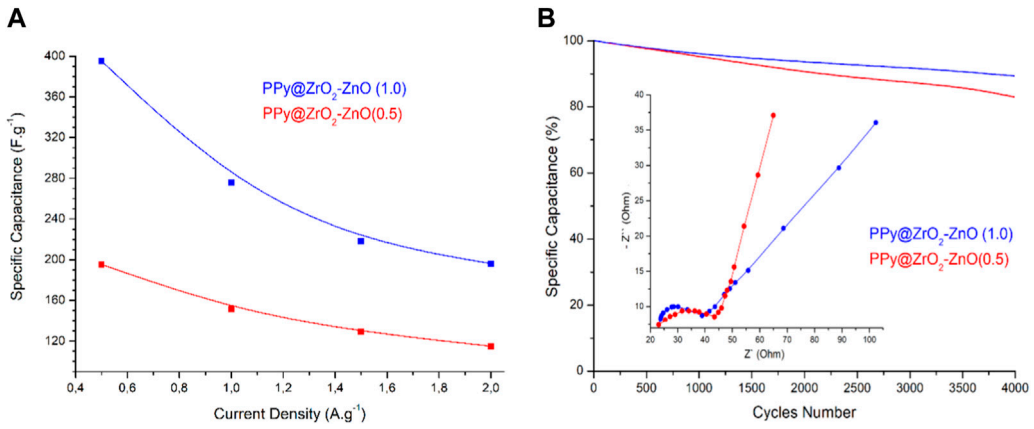

FIGURE 10
(A) Specific capacitance of electrodes at different current densities; **(B)** cycling stability of electrodes (0.5 A g^{-1}; 4,000 cycles) and the inset figure is the Nyquist plot.

TABLE 3 Electrochemical performance of some reported PPy-based electrodes.

Electrode material	Specific capacitance ($F{\cdot}g^{-1}$)	Energy density ($Wh{\cdot}kg^{-1}$)	Power density ($Wh{\cdot}kg^{-1}$)	Reference
PANI-RGO-ZnO	40.0	5.61	403	Palsaniya et al. (2021)
PPy/GO/ZnO	94.6	10.65	258.26	Chee et al. (2015)
rGO/$MnFe_2O_4$/PPy	232	32.3	581	Ishaq et al. (2019)
PPy	78–137	11–19	220–440	Tripathi et al. (2006)
MWCNT/PPy/MnO_2	270	36	500	Grover et al. (2014)
rGO/CNT/PPy	199	14	6,620	Peng et al. (2014)
Ag@TiO_2–ZrO_2	237	—	—	Sanu et al. (2023)
PPy@ZrO_2	337.83	187.68	1,000	Ullah et al. (2021)
PPy@ZrO_2–ZnO (1.0)	395.3	508.5	3,000	This work

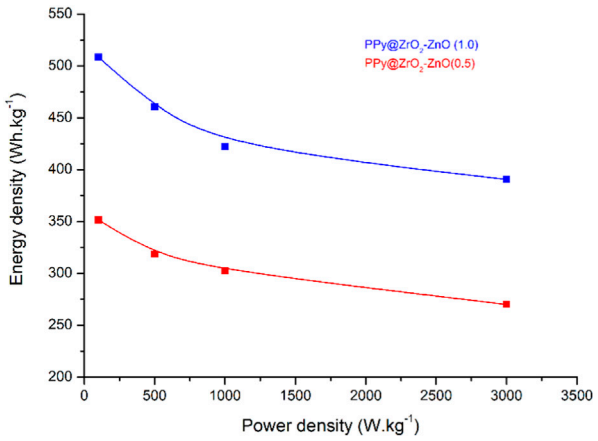

FIGURE 11
Ragone plots of the electrode at different current densities.

(1.0) presented longer discharge times than the electrodes of PPy@ZrO_2–ZnO (0.5). The prolonged discharge time is straight related to the higher energy density and larger specific capacity of the electrodes using PPy@ZrO_2–ZnO (1.0) (Figure 9A). Therefore, it is logical to conclude that a supercapacitor of PPy@ZrO_2–ZnO (1.0) is more adapted for empirical use than that of a PPy@ZrO_2–ZnO (0.5) electrode.

With increasing scan speeds, the electrolyte ion diffusion into electrodes becomes bit difficult, resulting in reduction of specific capacitance (C_g) of the sample. The (C_g) value of PPy@ZrO_2–ZnO (1.0) was around 395.3 F g^{-1}, which was preferable to the PPy@ZrO_2–ZnO (0.5) sample (195.3 F g^{-1}). These results could be due to the augmentation of conductivity but also due to the rise in surface areas. Moreover, at a power density of 100 $Wh{\cdot}kg^{-1}$, the energy densities of electrodes made from PPy@ZrO_2–ZnO (1.0) and PPy@ZrO_2–ZnO (0.5) were 508.5 and 351.5 $Wh{\cdot}kg^{-1}$, respectively. These energy densities of PPy@ZrO_2–ZnO (1.0) and PPy@ZrO_2–ZnO (0.5) electrodes were reduced to 390.6 and 270 $Wh{\cdot}kg^{-1}$, respectively, at a power density of 3,000 $W{\cdot}kg^{-1}$. This proves that as the power density augments, PPy@ZrO_2–ZnO (1.0) presents slower decreases in energy density relative to PPy@ZrO_2–ZnO (0.5). Consequently, PPy@ZrO_2–ZnO (1.0) not only stores more energy but also has good structural stability that enables the adsorption and desorption of ions (Cho et al., 2015; Hoseong Han et al., 2019).

The plot of specific capacitance at different discharge current densities is shown in Figure 10A. The capacitance of PPy@ZrO_2–ZnO (0.5) electrodes is 195.3 F g^{-1} at 0.5 A g^{-1} and 101.1 F g^{-1} at 2.0 A g^{-1}, with a capacitance retention of 51.7%. Interestingly, the capacitance of PPy@ZrO_2–ZnO (1.0) electrodes retains 80.01%, 66.7%, and 62.4% at 1.0, 1.5, and 2.0 A g^{-1}, respectively, *vs.* 395.3 F g^{-1} at 0.5 A g^{-1}. The ZrO_2–ZnO (1.0) ratio formed on the surface of PPy was key to enhancing the electrochemical performance of the electrode materials. With the increase in the discharge current density, the specific capacitance decreases gradually. In addition, the specific capacitances, energy densities, and power densities of electrodes were calculated at the current densities of 0.5, 1.0, 1.5, and 2.0 A g^{-1} based on the relevant formulas and GCD curves. On the other hand, the comparison of PPy electrode-based supercapacitors is shown in Table 3.

The electrochemical behavior of the two samples was also investigated by EIS to test its conductive behavior via the Nyquist plot, as shown in Figure 10B. In the low frequency, the straight line agrees with ion diffusion on the electrode/electrolyte surface (Conway, 2013). In the high-frequency zone, the semicircle diameter and intercept represent the charge transfer resistance and the equivalent series resistance, respectively (Conway, 2013). Clearly, the Nyquist plot revealed a minor semicircle arc on the real axis along with the vertical line for both electrodes, and shows that it has fast charge transport kinetics and low charge transfer resistance. Such a Nyquist diagram is a representation of the pseudo-capacitance behavior of electrodes (Wan et al., 2022; Ma et al., 2023), which is in perfect agreement with the CV and GCD studies discussed previously.

Ragone plots, which map the energy density and power density of electrodes by varying current densities (0.5, 1.0, 1.5, and 2.0 A g^{-1}), are demonstrated in Figure 11. It is seen that the PPy@ZrO_2–ZnO (0.5) electrode showed a relatively low energy density of 351.5 $Wh{\cdot}kg^{-1}$ with a power density of 100 W kg^{-1} at a current density of 0.5 A g^{-1}. Conversely, PPy@ZrO_2–ZnO (1.0) exhibited higher energy density of around 508.5 $Wh{\cdot}kg^{-1}$ with a

power density of 100 W kg^{-1} at a current density of 0.5 A g^{-1}. At a higher current density of 2.0 A g^{-1}, the energy densities of PPy@ZrO_2–ZnO (0.5) and PPy@ZrO_2–ZnO (1.0) electrodes decreased to 270.0 and 390.6 Wh·kg^{-1}, respectively.

To assure the supercapacitors' reliability, the long-term cycling stability of the electrodes was measured at a current density of 0.5 A·g^{-1} for 4,000 cycles under continuous GCD operation, as shown in Figure 10B. The retention rates of PPy@ZrO_2–ZnO (1.0) and PPy@ZrO_2–ZnO (0.5) were reduced to 9.8 and 17.6%, respectively.

4 Conclusion

In this study, PPy@ZrO_2–ZnO with different quantities of ZrO_2–ZnO (0.5 and 1.0) was synthesized and characterized by FTIR, XRD, XPS, UV-vis, BET, and TGA. Moreover, the CVs showed that the sample electrodes display pseudocapacitive properties. The specific capacitance values for PPy@ZrO_2–ZnO (1.0) and PPy@ZrO_2–ZnO (0.5) evaluated by galvanostatic discharge appeared as 395.3 and 195.3 F g^{-1} at 0.5 A g^{-1}, whereas the samples exhibited a value of energy density of 508.5 and 351.5 Wh·Kg^{-1}, respectively. The electrode stability for the synthesized samples was also investigated, which demonstrated specific capacitance retention at 90.2% for PPy@ZrO_2–ZnO (1.0) and 82.4% for PPy@ZrO_2–ZnO (0.5) after cycling up to 4,000 cycles.

Data availability statement

The original contributions presented in the study are included in the article/Supplementary Material, further inquiries can be directed to the corresponding authors.

Author contributions

Conceptualization: MZ and MK; data curation: AB; formal analysis: MK, AA, and AB; investigation: MZ, HB, MK, and YB; methodology: HB and YB; software: MZ, MA, and AA; validation: HB and MA; writing–original draft: MZ and AB; and writing–review and editing: YB. All authors contributed to the article and approved the submitted version.

Acknowledgments

The authors gratefully acknowledge the M.E.S.R.S. of Algerian and I.U.M.A. of Alicante University, Spain, for the cooperation availing. The authors extend their appreciation to the Deanship of Scientific Research at King Khalid University for funding this work through a large group Research Project under the grant number RGP2/358/44.

Conflict of interest

The authors declare that the research was conducted in the absence of any commercial or financial relationships that could be construed as a potential conflict of interest.

Publisher's note

All claims expressed in this article are solely those of the authors and do not necessarily represent those of their affiliated organizations, or those of the publisher, the editors, and the reviewers. Any product that may be evaluated in this article, or claim that may be made by its manufacturer, is not guaranteed or endorsed by the publisher.

References

Adam, K., Katarzyna, S. C., and Teofil, J. (2018). Titania-based hybrid materials with ZnO, ZrO_2 and MoS_2: a review. *Materials* 11, 2295. doi:10.3390/ma11112295

Anastassakis, E., Cantarero, A., and Cardona, M. (1990). Piezo-Raman measurements and anharmonic parameters in silicon and diamond. *Phys. Rev. B* 41, 7529–7535. doi:10.1103/PhysRevB.41.7529

Arote, S. A., Pathan, A. S., Hase, Y. V., Bardapurkar, P. P., Gapale, D. L., and Palve, B. M. (2019). Investigations on synthesis, characterization and humidity sensing properties of ZnO and ZnO-ZrO2 composite nanoparticles prepared by ultrasonic assisted wet chemical method. *Ultrason. Sonochemistry* 55, 313–321. doi:10.1016/j.ultsonch.2019.01.012

Augustyn, V., Simon, P., and Dunn, B. (2014). Pseudocapacitive oxide materials for high-rate electrochemical energy storage. *Energy and Environ. Sci.* 7, 1597–1614. doi:10.1039/C3EE44164D

Ayodeji, P. A., and Simón, Y. R. L. (2019). ZrO_2–ZnO nanoparticles as antibacterial agents. *ACS Omega* 4, 19216–19224. doi:10.1021/acsomega.9b02527

Azharudeen, A. M., Karthiga, R., Rajarajan, M., and Suganthi, A. (2020). Fabrication, characterization of polyaniline intercalated NiO nanocomposites and application in the development of non-enzymatic glucose biosensor. *Arabian J. Chem.* 13, 4053–4064. doi:10.1016/j.arabjc.2019.06.005

Belhadj, H., Moulefera, I., Sabantina, L., and Benyoucef, A. (2022). Effects of incorporating titanium dioxide with titanium carbide on hybrid materials reinforced with polyaniline: synthesis, characterization, electrochemical and supercapacitive properties. *Fibers* 10, 46. doi:10.3390/fib10050046

Benchikh, I., Dahou, F. Z., Lahreche, S., Sabantina, L., Benmimoun, Y., and Benyoucef, A. (2022). Development and characterisation of novel hybrid materials of modified ZnO-SiO_2 and polyaniline for adsorption of organic dyes. *Int. J. Environ. Anal. Chem.*, 1–20. doi:10.1080/03067319.2022.2107921

Bettucci, O., Matrone, G. M., and Santoro, F. (2022). Conductive polymer-based bioelectronic platforms toward sustainable and biointegrated devices: a journey from skin to brain across human body interfaces. *Adv. Mater. Technol.* 7, 2100293. doi:10.1002/admt.202100293

Bhattarai, R. M., Chhetri, K., Saud, S., Teke, S., Kim, S. J., and Mok, Y. S. (2022). Eco-friendly synthesis of cobalt molybdenum hydroxide 3d nanostructures on carbon fabric coupled with cherry flower waste-derived activated carbon for quasi-solid-state flexible asymmetric supercapacitors. *ACS Appl. Nano Mater.* 5, 160–175. doi:10.1021/acsanm.1c02354

Boutaleb, N., Dahou, F. Z., Djelad, H., Sabantina, L., Moulefera, I., and Benyoucef, A. (2022). Facile synthesis and electrochemical characterization of polyaniline@TiO2-CuO ternary composite as electrodes for supercapacitor applications. *Polymers* 14, 4562. doi:10.3390/polym14214562

Bryan, A. M., Santino, L. M., Lu, Y., Acharya, S., and D'Arcy, J. M. (2016). Conducting polymers for pseudocapacitive energy storage. *Chem. Mater.* 28, 5989–5998. doi:10.1021/acs.chemmater.6b01762

Chee, W. K., Lim, H. N., Harrison, I., Chong, K. F., Zainal, Z., Ng, C. H., et al. (2015). Performance of flexible and binderless polypyrrole/graphene oxide/zinc oxide supercapacitor electrode in a symmetrical two-electrode configuration. *Electrochimica Acta* 157, 88–94. doi:10.1016/j.electacta.2015.01.080

Ching, C. Y., Rahman, A., Ching, K. Y., Sukiman, N. L., and Cheng, H. C. (2015). Preparation and characterization of polyvinyl alcohol-based composite reinforced with nanocellulose and nanosilica. *BioResources* 10, 3364–3377. doi:10.15376/biores.10.2.3364-3377

Cho, S., Kim, M., and Jang, J. (2015). Screen-printable and flexible RuO2 nanoparticle-decorated PEDOT:PSS/graphene nanocomposite with enhanced

electrical and electrochemical performances for high-capacity supercapacitor. *ACS Appl. Mater. Interfaces* 7, 10213–10227. doi:10.1021/acsami.5b00657

Conway, B. E. (2013). *Electrochemical supercapacitors: Scientific fundamentals and technological applications*. Berlin, Germany: Springer Science and Business Media. ISBN 9781475730586.

Dubey, P., Maheshwari, P. H., and Sundriyal, S. (2022). Human hair-derived porous activated carbon as an efficient matrix for conductive polypyrrole for hybrid supercapacitors. *Energy and Fuels* 36, 13218–13228. doi:10.1021/acs.energyfuels.2c01926

Filho, U. P. R., Gushikem, Y., Fujiwara, F. Y., de Castro, S. C., Torriani, I. C. L., and Cavalcanti, L. P. (1994). Zirconium dioxide supported on.alpha.-Cellulose: synthesis and characterization. *Langmuir* 10, 4357–4360. doi:10.1021/la00023a070

Gautam, K. P., Acharya, D., Bhatta, I., Subedi, V., Das, M., Shova Neupane, S., et al. (2022). Nickel oxide-incorporated polyaniline nanocomposites as an efficient electrode material for supercapacitor application. *Inorganics* 10, 86. doi:10.3390/inorganics10060086

Grover, S., Shekhar, S., Sharma, R. K., and Singh, G. (2014). Multiwalled carbon nanotube supported polypyrrole manganese oxide composite supercapacitor electrode: role of manganese oxide dispersion in performance evolution. *Electrochim. Acta.* 116, 137–145. doi:10.1016/j.electacta.2013.10.173

Hammadi, F. Z., Belardja, M. S., Lafjah, M., and Benyoucef, A. (2021). Studies of influence of ZrO_2 nanoparticles on reinforced conducting polymer and their optical, thermal and electrochemical properties. *J. Inorg. Organomet. Polym. Mater.* 31, 1176–1184. doi:10.1007/s10904-020-01730-3

Han, H., and Cho, S. (2018). *Ex situ* fabrication of polypyrrole-coated core-shell nanoparticles for high-performance coin cell supercapacitor. *Nanomaterials* 8, 726. doi:10.3390/nano8090726

Handayani, M., Mulyaningsih, Y., Anggoro, M. A., Abbas, A., Setiawan, I., Triawan, F., et al. (2022). One-pot synthesis of reduced graphene oxide/chitosan/zinc oxide ternary nanocomposites for supercapacitor electrodes with enhanced electrochemical properties. *Mater. Lett.* 314, 131846. doi:10.1016/j.matlet.2022.131846

Hoseong Han, H., Lee, J. S., and Cho, S. (2019). Comparative studies on two-electrode symmetric supercapacitors based on polypyrrole:poly(4-styrenesulfonate) with different molecular weights of poly(4-styrenesulfonate). *Polymers* 11, 232. doi:10.3390/polym11020232

Huriya, H., Bushra, B., Salma, B., Anwar, U. H. A. S., and Philipp, R. (2023). Polyindole embedded nickel/zinc oxide nanocomposites for high-performance energy storage applications. *Nanomaterials* 13, 618. doi:10.3390/nano13030618

Ishaq, S., Moussa, M., Kanwal, F., Ehsan, M., Saleem, M., Van, T. N., et al. (2019). Facile synthesis of ternary graphene nanocomposites with doped metal oxide and conductive polymers as electrode materials for high performance supercapacitors. *Sci. Rep.* 9, 5974. doi:10.1038/s41598-019-41939-y

Jijie, W., Guanna, L., Zelong, L., Chizhou, T., Zhaochi, F., Hongyu, A. H. L., et al. (2017). A highly selective and stable ZnO-ZrO_2 solid solution catalyst for CO_2 hydrogenation to methanol. *Sci. Adv.* 3, 13394. doi:10.1126/sciadv.1701290

Kyunghwa Kim, K., An, J., Park, K., Roh, G., and Chun, K. (2019). Analysis of a supercapacitor/battery hybrid power system for a bulk carrier. *Appl. Sci.* 9, 1547. doi:10.3390/app9081547

Li, C., Hsu, Y. T., and Hu, W. W. (2016). The regulation of osteogenesis using electroactive polypyrrole films. *Polymers* 8, 258. doi:10.3390/polym8070258

Li, Z., Xie, X., Zhou, M., Zhu, L., Fu, C., and Chen, S. (2023). High water-stable, hard and strong-adhesive antistatic films from waterborne PEDOT:PSS composites. *Synth. Met.* 293, 117290. doi:10.1016/j.synthmet.2023.117290

Liang, W., Yang, W., Sakib, S., and Zhitomirsky, I. (2022). Magnetic CuFe2O4 nanoparticles with pseudocapacitive properties for electrical energy storage. *Molecules* 27, 5313. doi:10.3390/molecules27165313

Lim, Y. S., Tan, Y. P., Lim, H. N., Huang, N. M., Tan, W. T., Yarmo, M. A., et al. (2014). Potentiostatically deposited polypyrrole/graphene decorated nano-manganese oxide ternary film for supercapacitors. *Ceram. Int.* 40, 3855–3864. doi:10.1016/j.ceramint.2013.08.026

Ma, Q., Cui, F., Zhang, J., and Cui, T. (2023). Built-in electric field boosted ionic transport kinetics in the heterostructured $ZnCo_2O_4$/ZnO nanobelts for high-performance supercapacitor. *J. Colloid Interface Sci.* 629, 649–659. doi:10.1016/j.jcis.2022.09.013

Mahato, N., Debananda Mohapatra, D., Moo Hwan Cho, M. H., and Ahn, K. S. (2022). Semi-polycrystalline–polyaniline empowered electrochemical capacitor. *Energies* 15, 2001. doi:10.3390/en15062001

Mantione, D., Agua, I. D., Sanchez, A. S., and Mecerreyes, D. (2017). Poly(3,4-ethylenedioxythiophene) (PEDOT) derivatives: innovative conductive polymers for bioelectronics. *Polymers* 9, 354. doi:10.3390/polym9080354

Nolly, C., Ikpo, C. O., Ndipingwi, M. M., Ekwere, P., and Iwuoha, E. I. (2022). Pseudocapacitive effects of multi-walled carbon nanotubes-functionalised spinel copper manganese oxide. *Nanomaterials* 12, 3514. doi:10.3390/nano12193514

Obaidullah, M., Takeshi Furusawa, T., Siddiquey, I. A., Bahadur, N. M., Sato, M., and Suzuki, N. (2018). A fast and facile microwave irradiation method for the synthesis of ZnO@ZrO2 core-shell nanocomposites and the investigation of their optical properties. *Adv. Powder Technol.* 29, 1804–1811. doi:10.1016/j.apt.2018.04.016

Okhay, O., and Tkach, A. (2022). Synergetic effect of polyaniline and graphene in their composite supercapacitor electrodes: impact of components and parameters of chemical oxidative polymerization. *Nanomaterials* 12, 2531. doi:10.3390/nano12152531

Palsaniya, S., Nemade, H. B., and Dasmahapatra, A. K. (2021). Hierarchical PANI-RGO-ZnO ternary nanocomposites for symmetric tandem supercapacitor. *J. Phys. Chem. Solids* 154, 110081. doi:10.1016/j.jpcs.2021.110081

Parveen, N., Ansari, M. O., and Cho, M. H. (2016). Route to high surface area, mesoporosity of polyaniline–titanium dioxide nanocomposites via one pot synthesis for energy storage applications. *Industrial Eng. Chem. Res.* 55, 116–124. doi:10.1021/acs.iecr.5b02907

Peng, Y.-J., Wu, T.-H., Hsu, C.-T., Li, S.-M., Chen, M.-G., and Hu, C.-C. (2014). Electrochemical characteristics of the reduced graphene oxide/carbon nanotube/polypyrrole composites for aqueous asymmetric supercapacitors. *J. Power Sources* 272, 970–978. doi:10.1016/j.jpowsour.2014.09.022

Quintana, A., Altube, A., Lecina, E. G., Suriñach, S., Baró, M. D., Sort, J., et al. (2017). A facile co-precipitation synthesis of heterostructured ZrO2|ZnO nanoparticles as efficient photocatalysts for wastewater treatment. *J. Mater. Sci.* 52, 13779–13789. doi:10.1007/s10853-017-1488-5

Raveesha, H. R., Nayana, S., Vasudha, D. R., Begum, J. S., Pratibha, S., Ravikumara, C. R., et al. (2019). The electrochemical behavior, antifungal and cytotoxic activities of phytofabricated MgO nanoparticles using Withania somnifera leaf extract. *J. Sci. Adv. Mater. Devices* 4, 57–65. doi:10.1016/j.jsamd.2019.01.003

Rawal, I., Carey, J. D., Panwarde, O. S., and Tripathid, R. K. (2016). Organic–inorganic hybrid cathodes: facile synthesis of polypyrrole/zinc oxide nanofibers for low turn-on electron field emitters. *RSC Adv.* 6, 46372–46379. doi:10.1039/C6RA03449G

Rehman, M. M., Munawar, T., Nadeem, M. S., Mukhtar, F., Maqbool, A., Riaz, M., et al. (2021). Facile synthesis and characterization of conducting polymer-metal oxide based core-shell PANI-Pr_2O–NiO–Co_3O_4 nanocomposite: as electrode material for supercapacitor. *Ceram. Int.* 47, 18497–18509. doi:10.1016/j.ceramint.2021.03.173

Sanu, M. S., Prakashan, V. P., Sajna, M. S., Anoop, C., Gejo, G., Eric, K. B., et al. (2023). Development and characterizations of Ag nanoparticles decorated TiO_2-ZrO_2 coatings as electrode material for supercapacitors. *Results Surfaces Interfaces* 10, 100098. doi:10.1016/j.rsurfi.2023.100098

Selvi, N., Sankar, S., and Dinakaran, K. (2015). Interfacial effect: magnetism in pure ZrO_2, ZnO and SiO_2 coated core/shell/shell hybrid nanoparticles. *J. Mater. Sci. Mater. Electron.* 26, 273–279. doi:10.1007/s10854-014-2395-z

Shokufeh, A., Mona, M. T., and Shahin, A. (2021). Enhancing the photocatalytic properties of ZrO_2/ZnO nanocomposite supported on montmorillonite clay for photodegradation of Congo red. *J. Electron. Mater.* 50, 2870–2878. doi:10.1007/s11664-021-08805-y

Sirajul, H., Humma, A., Manel, B. A., Mohammed, A., Bander, A., and Amor, H. (2021). Green synthesis and characterization of a ZnO-ZrO_2 heterojunction for environmental and biological applications. *Crystals* 11, 1502. doi:10.3390/cryst11121502

Tripathi, S. K., Kumar, A., and Hashmi, S. A. (2006). Electrochemical redox supercapacitors using PVdF-HFP based gel electrolytes and polypyrrole as conducting polymer electrode. *Solid State Ionics* 177, 2979–2985. doi:10.1016/j.ssi.2006.03.059

Ullah, R., Khan, M., Khattak, R., Khan, N., Khan, M. S., and El-Badry, Y. A. (2021). Synthesis, characterization and evaluation of supercapacitive response of dodecylbenzenesulphonic acid (DBSA) doped polypyrrole/zirconium dioxide composites. *Polymers* 13, 4035. doi:10.3390/polym13224035

Umer, A., Liaqat, F., and Mahmood, A. (2020). MoO_3 nanobelts embedded polypyrrole/SIS copolymer blends for improved electro-mechanical dual applications. *Polymers* 12, 353. doi:10.3390/polym12020353

Wan, L., Jiang, T., Zhang, Y., Chen, J., Xie, M., and Du, C. (2022). 1D-on-1D core–shell cobalt iron selenide@cobalt nickel carbonate hydroxide hybrid nanowire arrays as advanced battery-type supercapacitor electrode. *J. Colloid Interface Sci.* 621, 149–159. doi:10.1016/j.jcis.2022.04.072

Wang, J., Wang, Z., Huang, B., Ma, Y., Liu, Y., Qin, X., et al. (2012). Oxygen vacancy induced band-gap narrowing and enhanced visible light photocatalytic activity of ZnO. *ACS Appl. Mater. Interfaces* 4, 4024–4030. doi:10.1021/am300835p

Xiangyu You, X., Misra, M., Gregori, S., and Mohanty, A. K. (2018). Preparation of an electric double layer capacitor (EDLC) using miscanthus-derived biocarbon. *ACS Sustain. Chem. Eng.* 6 (1), 318–324. doi:10.1021/acssuschemeng.7b02563

Yamani, K., berenguer, R., Benyoucef, A., and Morallón, E. (2019). Preparation of polypyrrole (PPy)-derived polymer/ZrO_2 nanocomposites: effects of nanoparticles interface and polymer structure. *J. Therm. Analysis Calorim.* 135, 2089–2100. doi:10.1007/s10973-018-7347-z

Zheng, H., Yan, Z., Wang, M., Chen, J., and Zhang, X. (2019). Biosensor based on polyaniline-polyacrylonitrile-graphene hybrid assemblies for the determination of phenolic compounds in water samples. *J. Hazard. Mater.* 378, 120714. doi:10.1016/j.jhazmat.2019.05.107